The incremental contribution of mobile cone-beam computed tomography to the tool–lesion relationship during shape-sensing robotic-assisted bronchoscopy

Bryan C. Husta [1], Anu Menon[1], Reza Bergemann[1], I-Hsin Lin[2], Jaclyn Schmitz[3], Rastko Rakočević[1], Tejaswi R. Nadig[1], Prasad S. Adusumilli [4], Jason A. Beattie[1], Robert P. Lee[1], Bernard J. Park [4], Gaetano Rocco[4], Matthew J. Bott [4], Mohit Chawla[1] and Or Kalchiem-Dekel [1]

[1]Section of Interventional Pulmonology, Pulmonary Service, Memorial Sloan Kettering Cancer Center, New York, NY, USA. [2]Department of Epidemiology and Biostatistics, Memorial Sloan Kettering Cancer Center, New York, NY, USA. [3]Department of Medical Physics, Memorial Sloan Kettering Cancer Center, New York, NY, USA. [4]Thoracic Surgery Service, Department of Surgery, Memorial Sloan Kettering Cancer Center, New York, NY, USA.

Corresponding author: Bryan C. Husta (hustab@mskcc.org)

Shareable abstract (@ERSpublications)
This is the first study to demonstrate a significant qualitative and quantitative improvement in achieving tool-in-lesion status in robotic bronchoscopy and mobile cone-beam computed tomography https://bit.ly/42RZp8B

Abstract

Introduction This study aims to answer the question of whether adding mobile cone-beam computed tomography (mCBCT) imaging to shape-sensing robotic-assisted bronchoscopy (ssRAB) translates into a quantifiable improvement in the tool–lesion relationship.

Methods Data from 102 peripheral lung lesions with $\geqslant 2$ sequential mCBCT orbital spins and from 436 lesions with 0–1 spins were prospectively captured and retrospectively analysed. The primary outcome was the tool–lesion relationship status across the first and the last mCBCT spins. Secondary outcomes included 1) the change in distance between the tip of the sampling tool and the centre of the lesion between the first and the last spins and 2) the per-lesion diagnostic yield.

Results Compared to lesions requiring 0–1 spins, lesions requiring $\geqslant 2$ spins were smaller and had unfavourable bronchus sign and intra-operative sonographic view. On the first spin, 54 lesions (53%) were designated as non-tool-in-lesion (non-TIL) while 48 lesions (47%) were designated as TIL. Of the 54 initially non-TIL cases, 49 (90%) were converted to TIL status by the last spin. Overall, on the last spin, 96 out of 102 lesions (94%) were defined as TIL and six out of 102 lesions (6%) were defined as non-TIL (p<0.0001). The mean distance between the tool and the centre of the lesion decreased from 10.4 to 6.6 mm between the first and last spins (p<0.0001). The overall diagnostic yield was 77%.

Conclusion Targeting traditionally challenging lung lesions, intra-operative volumetric imaging allowed for the conversion of 90% of non-TIL status to TIL. Guidance with mCBCT resulted in a significant decrease in the distance between the tip of the needle to lesion centre.

Introduction

Rates of detection and sampling of pulmonary lesions has increased significantly over the past two decades, primarily owing to widespread use of computed tomography (CT) and implementation of lung cancer screening guidelines [1]. Within the context of lung cancer, American College of Chest Physicians guidelines recommend bronchoscopy for tissue acquisition because it allows for concomitant mediastinal lymph node staging [2]; however, the diagnostic yield of legacy guided bronchoscopy platforms has been relatively low at a range of 65–73% [3–6]. While the safety profile of guided bronchoscopy in terms of pneumothorax and bleeding is superb, its diagnostic yield rate remains inferior compared to the alternative approach of transthoracic image-guided sampling [6–10].

Robotic-assisted bronchoscopy (RAB) was developed to overcome legacy platform shortcomings, while maintaining an excellent safety profile. Early reports of diagnostic yield rates for RAB were within the range of 69–86% [11–15]. The remaining gap in diagnostic yield between RAB and percutaneous sampling is primarily attributed to CT-to-body divergence [16]. To overcome CT-to-body divergence, feedback provided by intra-operative volumetric imaging allows for the performance of real-time micro-adjustments to improve the tool–lesion relationship. Cone-beam CT (CBCT) imaging was recently integrated into RAB to allow precise intra-operative visualisation of the tool–lesion relationship [17, 18]. Mobile CBCT (mCBCT) integrates intra-operative volumetric imaging with mobility, but without the augmented fluoroscopy module provided by fixed CBCT systems [17, 19, 20].

The combination of RAB and mCBCT can enhance the confidence in tissue acquisition through visualisation of tool-in-lesion (TIL), but the value of mCBCT in improving the tool–lesion relationship during RAB has yet to be extensively determined [19]. In this study, we aimed to quantify the incremental contribution of mCBCT imaging to improving the tool–lesion relationship and achieving TIL status when used in conjunction with shape-sensing RAB (ssRAB). Our *a priori* hypothesis was that in procedures where multiple mCBCT scans (*i.e.* "spins") were performed to guide catheter adjustment, the tool–lesion relationship would improve between the first and last spins. Additionally, we examined the relationship between TIL status and diagnostic yield.

Study design and methods

Participant, lesion and procedure data

Data were acquired from a prospectively curated research electronic data capture (REDCap) database [21] of all ssRAB cases performed at Memorial Sloan Kettering Cancer Center (MSK). All patients who underwent mCBCT-guided ssRAB for the sampling of lung lesions between August 2020 and February 2022 were eligible for this study. This Health Insurance Portability and Accountability Act-compliant study was approved by the MSK institutional review board (protocol identifier: 20–102).

The pre-operative CT was reviewed by two of the study authors (BCH and OK-D). Lesion size was determined as the largest dimension in axial, sagittal and coronal projections. Centrality within the lung parenchyma was determined by dividing the lung into an inner two thirds and an outer one third [22]. A positive bronchus sign was defined by the presence of an airway leading to the lesion or coursing through it as an air bronchogram [23]. ssRAB (Ion Robotic-Assisted Endoluminal Platform; Intuitive Surgical Inc., Sunnyvale, CA, USA) was performed by one of nine users as described previously [14]. Briefly, all procedures were performed under general anaesthesia and mechanical ventilation with 10 mL·kg^{-1} tidal volumes, positive end-expiratory pressure of 10 cmH$_2$O and fraction of inspired oxygen of 30–40%, as tolerated by the patient [24, 25]. Following navigation to the target lesion, radial probe endobronchial ultrasound (rpEBUS) (UM-S20-17S or UM-S20-20R-3; Olympus Corp., Tokyo, Japan) was deployed at the operator's discretion. The sonographic image was classified as concentric, eccentric or no view, with the best view acquired prior to sampling recorded [26]. Sampling was performed using a cytology needle (Flexision; Intuitive Surgical Inc.) in all cases. Needle gauge as well as use of any additional sampling tools were left to the discretion of the operator. Intra-operative fluoroscopic imaging was accomplished with the Cios Spin Mobile 3D C-Arm (Siemens Healthineers Inc., Erlangen, Germany). Pulsed two-dimensional (2D) fluoroscopy was used in all cases. mCBCT orbital scans (*i.e.* spins) were performed at the discretion of the operator and under a breath hold using a "standard" imaging protocol and "soft tissue" algorithm, as defined by the manufacturer. Axial, sagittal and coronal projection images were reformatted and reviewed intra-operatively [27]. At the discretion of the operator, the robotic catheter was then re-directed to augment tool–lesion approximation. This process was repeated, and additional spins were acquired as needed to achieve optimal TIL status. Of note, this study was performed prior to the formal integration of the Ion Cios Spin systems that allow for intra-operative target updating. Sampling was undertaken once the most satisfactory position was achieved. Rapid on-site evaluation of cytology material was employed in all cases.

Tool–lesion relationship and distance measurements

The tool–lesion relationship was determined for cases in which mCBCT spin images were acquired. The study cohort was dichotomised based on the number of mCBCT spins performed during the procedure. Cases that included two or more spins per target were grouped into the Primary Outcome cohort, while cases that included none or a single spin were grouped into the Comparison cohort. As illustrated in figure 1, the tool–lesion relationship was defined by analysis of the intra-operative mCBCT images, using Mimics Innovation Suite 25.0 and Materialise 3-matic Medical version 17.0 (both Materialise, Leuven, Belgium). As a proof of concept, this method for quantitating (*i.e.* TIL *versus* non-TIL) and quantifying (*i.e.* distance measurement) of the tool–lesion relationship was verified using the ATOM Radiology
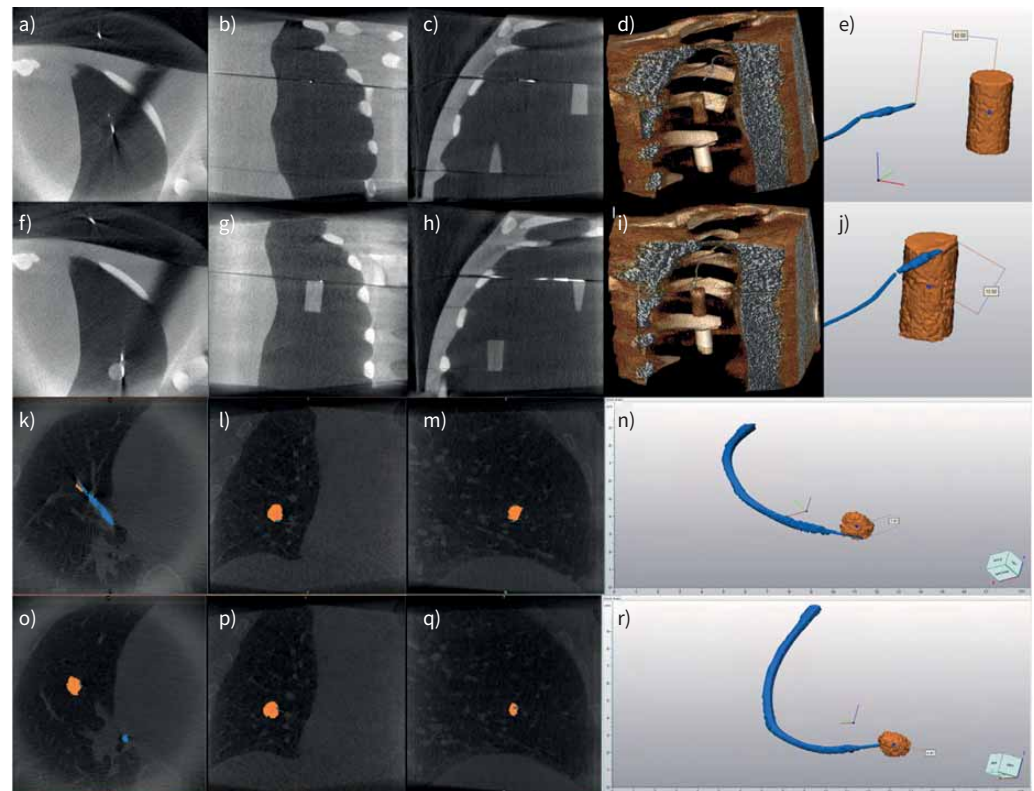
FIGURE 1 Phantom model-based proof of concept (a–j) and illustrative patient case (k–r) for lesion and needle segmentation, definition of lesion volumetric centre and tip of the needle-to-lesion volumetric centre distance measurement. Volumetric imaging was obtained using the Cios Spin Mobile 3D C-Arm (Siemens Healthiness Inc., Erlangen, Germany) using a "standard" imaging protocol and "soft tissue" algorithm as defined by the manufacturer. A non-tool-in-lesion (non-TIL) and a tool-in-lesion (TIL) condition were simulated using the ATOM Radiology Phantom Adult Male Model #701 and a 21G transbronchial needle (Wang 21G Transbronchial Cytology Needle, ConMed, Utica, NY, USA). Images in the axial, coronal and sagittal planes were then reformatted into DICOM files. The unprocessed computed tomography images in DICOM format were loaded into Mimics Innovation Suite 25.0 (Materialise, Leuven, Belgium). A mask was then generated based on radio density thresholding, which was adjusted to ensure the most complete segmentation of both catheter and needle. A region grow was performed to remove any voxels included in the model that were not part of the catheter and needle. The mask was then edited in each plane to correct for artefacts and mistakes in the thresholding. A second mask was generated with the boundaries confined to the area of the target lesion and the threshold adjusted to ensure complete segmentation. A region grow was then performed to eliminate voxels that fell within the threshold but were not connected to the mass. Again, the mask was edited in each plane to correct for any unintentionally included or excluded voxels in the model. Each of the masks was then converted to triangulated surface mesh files, which were exported to Materialise 3-matic Medical version 17.0 (Materialise) for finite element analysis. For each target lesion, a centroid point was generated to approximate the volumetric centre for the lesion mesh. A measurement in millimetres was taken from the distal-most point on the needle to the centroid of the mass. a–j) Simulation. a–c, f–h) Unprocessed DICOM images in the axial (a, f), coronal (b, g) and sagittal (c, h) planes, illustrating the needle-to-lesion relationship in a non-TIL (a–c) and TIL (f–h) status. d, i) Three-dimensional reconstruction of axial, coronal and sagittal images, illustrating the needle-to-lesion relationship in a non-TIL (d) and a TIL (i) status. e, j) Mask image after segmentation of the needle (blue) and the lesion (orange), determination of the lesion's volumetric centre (blue dot), and distance measurement between the tip of the needle and the volumetric centre. Images illustrate the tip of the needle-to-volumetric centre distance measurement in a non-TIL (e) and a TIL (j) status. k–r) Patient case. k–m) Initial mobile cone-beam CT spin images in the axial (k), coronal (l) and sagittal (m) projections along with segmentation of the needle (blue) and target lesion (orange). The tool–lesion relationship was classified as non-TIL. n) After identification of the lesion's volumetric centre (blue dot), the distance between the tip of the needle and the volumetric centre was determined as 7.81 mm. o–q) Final mobile cone-beam CT spin images in the axial (o), coronal (p) and sagittal (q) projections along with segmentation of the needle (blue) and target lesion (orange) after adjustments to the robotic catheter. The tool–lesion relationship was classified as TIL. r) The distance between the tip of the needle and the volumetric centre was determined as 4.87 mm.

Phantom Adult Male Model #701. In brief, a three-dimensional (3D) model was generated to 1) segment the needle and the target lesion, 2) identify the lesion's volumetric centre, 3) identify the tip of the needle, 4) define the tool–lesion relationship and 5) measure the distance between the tip of the needle and the target lesion's volumetric centre. In cases in which two or more spins were performed, this process was repeated for the initial and final mCBCT spin images across all lesions included in this study. The volumetric images were independently reviewed by two of the study authors (BCH and OK-D) and the tool–lesion relationship on the first and last spin images was classified as either TIL or non-TIL. TIL was considered achieved if the tip of the sampling tool was completely surrounded by the lesion in multiple projections. For cases of multiple spins, the sampling outcome was then stratified based on the first to last spin tool–lesion relationship as TIL–TIL, non-TIL–TIL, TIL–non-TIL and non-TIL–non-TIL (supplementary figures S1–S4). The distance between the tip of the needle the lesion's volumetric centre as well as TIL status were then measured on the first and final spin for each given target (figure 1).

Outcome measures

The primary outcome measure of this study was the tool–lesion relationship status between the initial and final mCBCT spins. Secondary outcomes included 1) the difference in distance between the tip of the needle and the volumetric centre of the lesion between the first and last spins as well as 2) the per-lesion diagnostic yield. Diagnostic yield was determined as described previously [14]. Lesions were classified as malignant, non-malignant or insufficient, based on the cytology and pathology analysis. All malignant lesions were considered diagnostic, unless proven to be false positive on subsequent surgical resection. All insufficient samplings and samplings showing only undifferentiated atypical cells were designated non-diagnostic. Non-malignant lesions were considered diagnostic if 1) the diagnosis was confirmed *via* an alternative sampling modality, such as percutaneous biopsy or surgical resection; or 2) follow-up imaging demonstrated either regression of the lesion or stability over ⩾12 months. This definition of diagnostic sampling is aligned with "method 3" as described by VACHANI *et al.* [28] or the "intermediate" definition as described by LEONARD *et al.* [29].

Statistical analysis

Descriptive statistics are presented as n (%) for categorical variables, and as median (interquartile range (IQR)) for continuous variables. To compare patient, lesion and procedural characteristics between the Primary Outcome cohort and the Comparison cohort as well as between diagnostic and non-diagnostic lesions, the t-test or Mann–Whitney–Wilcoxon U test was performed for continuous variables, and the Chi-square or Fisher's exact test for categorical variables. The tool–lesion relationship status between the initial spin to the final spin was compared using the exact McNemar's test. Wilcoxon signed-rank test was used to compare the median difference between the initial and final distance between the tip of the needle and the centre of the lesion. For the Primary Outcome cohort, a logistic regression model was used to evaluate associations of radiographic and procedural characteristics with the diagnostic yield. Variables were selected based on prior studies showing their relevance in predicting diagnostic yield [8, 9, 11, 13, 14, 17]. All statistical tests were two-tailed, and a p-value of <0.05 was considered statistically significant. SAS software (version 9.4; SAS Institute Inc., Cary, NC, USA) was used for all analyses.

Results

Study participants, lesions and procedures

The study case workflow chart is illustrated in supplementary figure S5. During the study period, a total of 612 lesions were targeted by 535 mCBCT-guided ssRAB procedures. In 381 of these procedures, encompassing 436 targeted lesions, none or one mCBCT spin were performed; this comprised the Comparison cohort. Two cases were subsequently excluded from the Comparison cohort as they included fiducial deployment only without target sampling. A total of 154 cases included ⩾2 spins per target. Of these, we excluded 58 procedures owing to incomplete mCBCT imaging data. Ultimately, the Primary Outcome cohort included 96 procedures, performed on 95 patients (one patient underwent two procedures) and encompassing 102 lesions.

Demographic, anthropometric and clinical characteristics of the two study cohorts are presented in table 1. The mean age was 68±12 years and 58% were female. The Primary Outcome and Comparison cohorts were similar in terms of patient characteristics. Target lesion radiographic and intra-operative characteristics are presented in table 2. Compared with the Comparison cohort (0–1 spins), target lesions in the Primary Outcome cohort (⩾2 spins) were smaller in median diameter (15.8 *versus* 22.6 mm; p<0.001), had a lower prevalence of positive bronchus sign (29% *versus* 60%; p<0.001), a lower prevalence of concentric rpEBUS view (20% *versus* 45%) and a higher prevalence of "no view" on rpEBUS (39% *versus* 15%).

TABLE 1 Patient characteristics				
Variable	Collective study cohorts	Individual study cohorts		
		Primary Outcome cohort (⩾2 spins)	Comparison cohort (0–1 spins)	p-value
Patients (n)	474	95	379	
Age (years)	68±12	68±11	68±12	0.9
Female sex	274 (58)	54 (57)	220 (58)	0.8
Smoking status				0.9
Never-smoker	143 (30)	30 (32)	113 (30)	
Ever-smoker	331 (70)	65 (68)	266 (70)	
Current	52 (16)	10 (15)	42 (16)	
Former	279 (84)	55 (85)	224 (84)	
Comorbidities				
Hypertension	229 (48)	47 (49)	182 (48)	0.8
Obstructive lung disease	130 (27)	20 (21)	110 (29)	0.1
Coronary artery disease	67 (14)	16 (17)	51 (14)	0.4
Diabetes mellitus	52 (14)	14 (15)	66 (14)	0.8
Obstructive sleep apnoea	32 (8)	9 (9)	41 (8)	0.8
Chronic kidney disease	10 (2)	4 (4)	6 (3)	0.06
Heart failure	9 (2)	2 (2)	7 (2)	0.3
Interstitial lung disease	3 (1)	1 (1)	2 (1)	0.4
Cerebrovascular accident	13 (3)	1 (1)	12 (3)	0.2
Prior history of cancer				
None	95 (20)	18 (19)	77 (20)	0.8
Primary thoracic	98 (20)	19 (20)	79 (21)	0.7
Primary extra-thoracic	281 (59)	58 (61)	223 (59)	0.6

Data are presented as mean±SD or n (%), unless otherwise indicated.

Tool–lesion relationship

Across the two study cohorts, the rate of TIL documentation was similar (table 2). In the Primary Outcome cohort (⩾2 spins), a mean of 3±1.2 spins were performed per lesion. As illustrated in figure 2, of the total of 102 lesions, 54 (53%) were designated as non-TIL and 48 lesions (47%) were designated as TIL on the first spin. Of the 54 initially non-TIL lesions, in 49 lesions (90.7%) a TIL status was documented on the final spin (*i.e.* non-TIL–TIL) while five (9.3%) remained as non-TIL (*i.e.* non-TIL–non-TIL). Of the 48 lesions that were initially designated TIL, 47 (97.9%) remained so by the last spin (*i.e.* TIL–TIL) and one (2.1%) converted to a non-TIL status (*i.e.* TIL–non-TIL). Overall, based on the last spin, 96 out of 102 lesions (94%) were defined TIL and six out of 102 lesions (6%) were defined as non-TIL. Comparison of the first and the last spin tool–lesion relationship status revealed a statistically significant increase in the rate of TIL status on the final spin (p<0.0001; supplementary table S1). Lesion characteristics stratified by tool–lesion relationship are shown in table 3.

As illustrated in figure 3a, the mean distance from the tip of the needle to the volumetric centre of the target lesion decreased from 10.4±5.1 mm on the first spin to 6.6±3.7 mm on the final spin (p<0.00001), reflecting a mean decrease in distance of 3.7±4.1 mm. A decrease in the distance of 2.2±3.2 mm and 4.9±4.6 was also observed within the subgroups of TIL–TIL and non-TIL–TIL lesions, respectively (figure 3b and supplementary figure S6).

Diagnostic yield

As shown in table 2, the overall diagnostic yield across the full study cohort was 77%. Diagnostic yield was similar between the Primary Outcome and Comparison cohorts with rates of 72% and 78%, respectively (p=0.17). There was no difference between the two cohorts in terms of malignant *versus* non-malignant diagnostic samplings (p=0.23). A depiction of the breakdown of the pulmonary lesion aetiologies across the Primary Outcome cohort is illustrated in supplementary figure S7. The diagnostic yield rates for the Comparison cohort stratified by TIL status are provided in the supplementary appendix. Diagnostic yield rates for the Primary Outcome cohort stratified by first to last spin tool–lesion relationships are shown in figure 2. While the diagnostic yield rates for TIL–TIL and non-TIL–TIL lesions were 72% and 76%, respectively, the yield for non-TIL–non-TIL lesions was 40%. Diagnostic yield rates

TABLE 2 Lesion characteristics				
Variable	Collective study cohorts	Individual study cohorts		
		Primary Outcome cohort (⩾2 spins)	Comparison cohort (0–1 spins)	p-value
Lesions (n)	538	102	436	
Size (mm)	21.0 (14.7–32.1)	15.8 (11.0–21.0)	22.6 (1.55–3.49)	<0.001
Radiographic consistency				0.5
Solid	356 (66)	65 (64)	291 (67)	
Ground glass	43 (8)	9 (9)	34 (8)	
Mixed	86 (16)	17 (17)	69 (16)	
Other	53 (10)	11 (10)	42 (10)	
Lobar location				0.5
Upper lobe	309 (57)	61 (60)	248 (57)	
Non-upper lobe	229 (43)	41 (40)	188 (43)	
Centrality				0.5
Inner 2/3	309 (57)	51 (50)	248 (57)	
Outer 1/3	229 (43)	51 (50)	188 (43)	
Radial EBUS				
Utilised	403 (75)	90 (88)	313 (72)	<0.001
Concentric	158 (40)	18 (20)	140 (45)	
Eccentric	161 (40)	37 (41)	124 (40)	
No view	84 (20)	35 (39)	49 (15)	
Not utilised	135 (25)	12 (12)	123 (28)	
Positive bronchus sign	294 (55)	30 (29)	264 (60)	<0.001
Number of traversed airway generations	7 (6–8)	7 (6–8)	7 (6–8)	1.0
Number of spins performed	1 (0–1)	3 (2–3)	1 (0–1)	<0.001
TIL documented	333 (92)	96 (95)	237 (91)	0.1
Diagnostic sampling	413 (77)	73 (72)	340 (78)	0.2
Malignant	279 (67)	45 (62)	234 (69)	
Non-malignant	134 (33)	28 (38)	106 (31)	
Complications[#]				n/a
Pneumothorax	1 (0.2)	0 (0.0)	1 (0.2)	
Pneumothorax requiring drainage	1 (0.2)	0 (0.0)	1 (0.2)	
Significant bleeding	1 (0.2)	0 (0.0)	1 (0.2)	

Data are presented as median (interquartile range) or n (%), unless otherwise indicated. EBUS: endobronchial ultrasound; TIL: tool-in-lesion. [#]: per-procedure analysis on a total of 486 procedures, 96 of which were included in the Primary Outcome cohort and 379 of which were performed on the Comparison cohort.

stratified by lesion size are illustrated in supplementary figure S8. Supplementary table S2 illustrates the radiographic characteristics across diagnostic and non-diagnostic samplings. Results of the logistic regression model evaluating associations of radiographic and procedural characteristics with the diagnostic yield across the Primary Outcome cohort are presented in table 4. Compared to non-TIL status on the last spin, TIL status on the last spin was associated with a 5.68-fold increase in the odds ratio for a diagnostic sampling (95% CI 0.98–32.93, p=0.053).

Safety

Across 475 procedures included in both study cohorts there was once instance of procedure-related significant bleeding (0.2%) and one instance of pneumothorax (0.2%), requiring placement of a chest tube. Both complications occurred in the Comparison cohort. There were no instances of early procedure termination or death recorded.

Discussion

RAB has empowered clinicians to safely access pulmonary lesions with greater confidence and accuracy, leading to increased interest in further development of this technology [11, 14, 15, 17, 20, 30]. In this study, we explore, quantify and quantitate the incremental value of integrating mCBCT with ssRAB for the achievement of TIL status. We are the first to demonstrate that the incorporation of mCBCT into ssRAB allowed for the conversion of 90.7% of initially non-TIL sampling attempts into TIL by guiding the
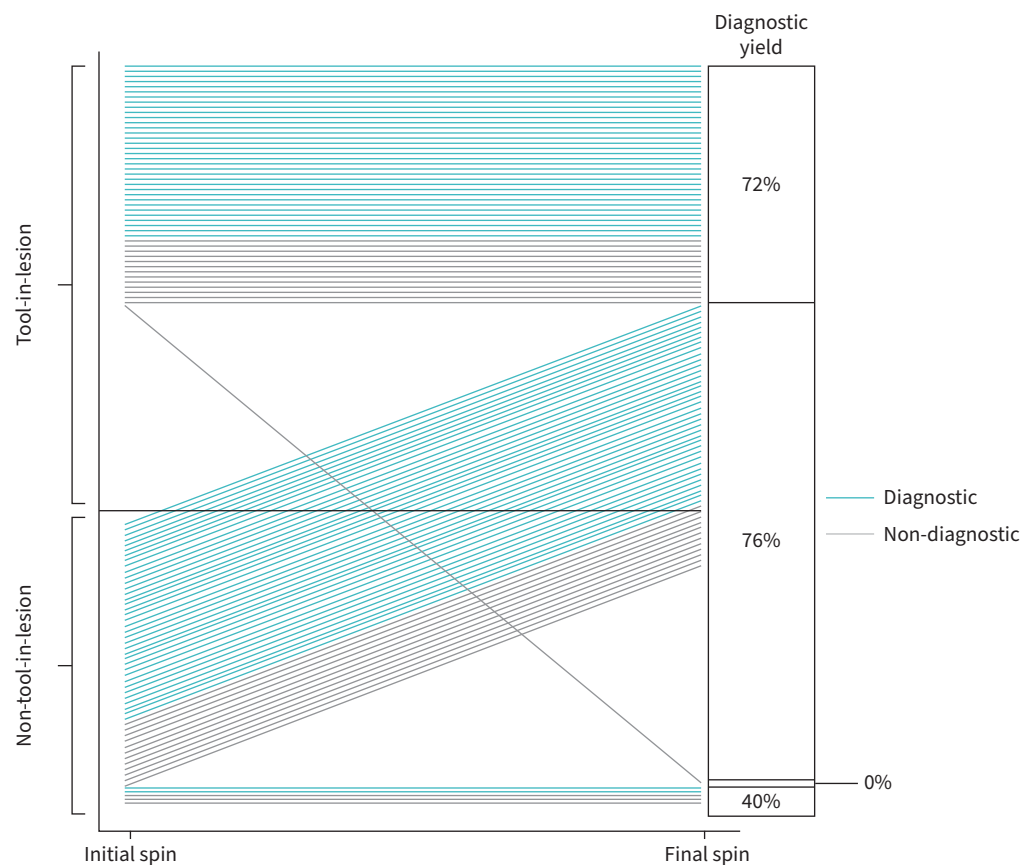
FIGURE 2 Tool–lesion relationship on initial and final mobile cone-beam computed tomography (mCBCT) spins along with the corresponding rates of diagnostic yield by group. In this line plot, each line represents one lesion. The tool–lesion relationship (x-axis) is demonstrated across the initial and final mCBCT spins (y-axis). The line trajectories create four outcome groups: TIL–TIL, non-TIL–TIL, non-TIL–non-TIL and TIL–non-TIL. The diagnostic yield for each group is represented by line colouring as well as a rate on the right-hand side, except for the TIL–non-TIL group (n=1). TIL: tool-in-lesion.

refinement of the tool–lesion relationship. This is the first study to demonstrate that mCBCT-guided catheter adjustments result in a statistically significant decrease in the distance between the tip of the needle and the volumetric centre of the lesion. This decrease was more prominent in non-TIL–TIL lesions compared with TIL–TIL lesions.

Real-time intra-procedural manipulation of the catheter loaded with a sampling tool and confirmation of TIL using adjunct imaging modalities has the potential to overcome some of the current challenges associated with navigational bronchoscopy. Furthermore, it may hold the key to increased confidence in the accuracy of diagnostic material obtained from the target lesion. Consequently, there has been significant interest in combining navigational bronchoscopy platforms with intra-procedural volumetric imaging [17–20, 31].

Regardless of bronchoscopy platform, navigational systems aid in enhancing the bronchoscopist's understanding of the respiratory tree anatomy, thus augmenting procedural capabilities. The navigation pathway is planned in advance using a virtual roadmap that is based on a pre-operative CT scan, usually performed at end-inspiration to best approximate the lung volume at total lung capacity. This allows for optimal airway segmentation to achieve both accuracy and detail. However, an impediment arises with alterations in intra-procedural lesion localisation due to the changes in lung anatomy that are induced by mechanical ventilation. These changes lead to discrepancies between the estimation of the virtual target and the real-time target location, termed CT-to-body divergence. CT-to-body divergence has been previously shown to impact diagnostic accuracy, especially in smaller, distal and lower lobe-located targets [16, 32].

TABLE 3 Comparison of lesion characteristics across the tool–lesion relationship groups within the Primary Outcome cohort

Variable	Tool–lesion relationship		
	TIL–TIL	Non-TIL–TIL	Non-TIL–non-TIL
Lesions[#] (n)	47	49	5
Size (mm)	17.0 (13.0–22.1)	15.0 (11.0–21.0)	10.3 (9.0–28.1)
Radiographic consistency			
Solid	29 (62)	34 (70)	2 (40)
Ground glass	4 (8)	4 (8)	1 (20)
Mixed	9 (19)	7 (14)	1 (20)
Other	5 (11)	4 (8)	1(20)
Lobar location			
Upper lobe	31 (66)	26 (53)	2 (40)
Non-upper lobe	16 (34)	23 (47)	3 (60)
Centrality			
Inner 2/3	25 (53)	22 (45)	4 (80)
Outer 1/3	22 (47)	27 (55)	1 (20)
Radial EBUS			
Utilised	40 (85)	45 (92)	4 (80)
Concentric	6 (15)	11 (24)	1 (25)
Eccentric	18 (45)	17 (38)	1 (25)
No view	16 (40)	17 (38)	2 (50)
Not utilised	7 (15)	4 (8)	1 (20)
Positive bronchus sign	15 (32)	13 (27)	2 (40)
Number of traversed airway generations	7 (6–8)	7 (7–8)	7 (6.5–7.5)

Data are presented as median (interquartile range) or n (%), unless otherwise indicated. EBUS: endobronchial ultrasound; TIL: tool-in-lesion. [#]: n=101, TIL–non-TIL status was documented in one case and data therefore not shown.
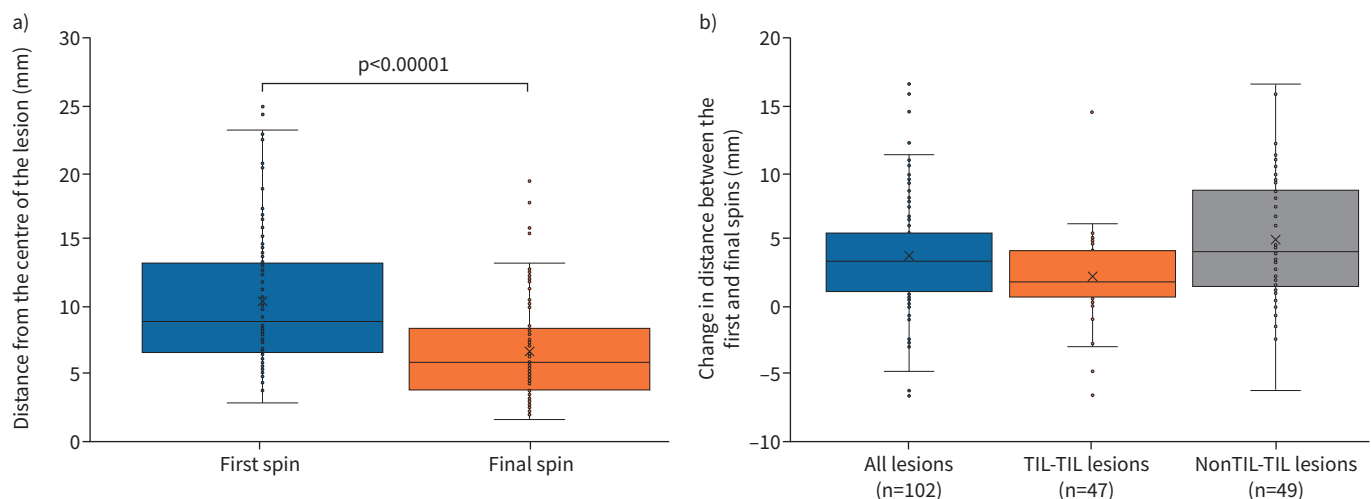
FIGURE 3 The change in distance from the tip of the needle to the volumetric centre of the lesion between the first and final mobile cone-beam computed tomography spins. a) The box-and-whisker plot describes the distribution of the median distance between the tip of the needle and the volumetric centre of the lesion for the initial and final spins across all lesions and stratified by tool–lesion relationship. Wilcoxon signed-rank test was used to compare the median difference between the initial and final distance between the tip of the needle and the centre of the lesion. b) The box-and-whisker plot describes the distribution of the change in median distance between the tip of the needle and the centre of the lesion between the initial and final spins across all lesions and stratified by tool–lesion relationship. Data not shown for the non-TIL–non-TIL and TIL–non-TIL groups owing to the small number of observations (n=5 and n=1, respectively). For both a and b, the "×" inside each box represents the mean and the line inside each box represents the median. The surrounding box represents the interquartile range. The lower whisker extends from the 25th to the 5th percentile and the upper whisker extends from the 75th to the 95th percentile. TIL: tool-in-lesion.

TABLE 4 Association between radiographic and procedural characteristics and diagnostic yield

		Univariate model		Multivariable model	
		OR (95% CI)	p-value	OR (95% CI)	p-value
Tool–lesion relationship on final mCBCT spin	Non-TIL	1.0		1.0	
	TIL	5.68 (0.98–32.93)	0.053	5.27 (0.89–31.17)	0.07
Lesion size	<20 mm	1.0		1.0	
	⩾20 mm	1.37 (0.53–3.52)	0.52	1.40 (0.53–3.69)	0.50
Radial EBUS view	No view	1.0			
	Any view	1.12 (0.42–2.98)	0.82		

mCBCT: mobile cone-beam computed tomography; EBUS: endobronchial ultrasound; TIL: tool-in-lesion.

rpEBUS and conventional 2D fluoroscopy have been used intra-operatively to improve the tool–lesion relationship; however, these tools provide limited information [33]. The value of conventional 2D fluoroscopy is limited in very small or ground glass consistency targets [33]. Regardless of lesion size or consistency, by virtue of providing only 2D images, conventional fluoroscopy is unable to confirm the precise volumetric spatial relationship of the sampling tool with the target lesion [34]. While augmented fluoroscopy and tomosynthesis-based fluoroscopic navigation platforms provide better understanding of 3D intra-operative spatial relationships, studies of these systems remain small and are limited to high-volume single-centre experiences and their image resolution remains inferior to that provided by CBCT platforms [35–38]. rpEBUS provides valuable confirmatory information when showing a concentric sonographic view. While an eccentric sonographic view is also valuable, it cannot be used to guide directionality. The role of rpEBUS in lesions without a leading or adjacent airway or in "no view" sonographic image is limited [39]. Indeed, in the Primary Outcome cohort of our study, 80% of rpEBUS images were unfavourable in terms of guiding sampling, *e.g.* eccentric or no view. Furthermore, conventional rpEBUS does not provide real-time TIL confirmation. Although a real-time rpEBUS-guided sampling needle was recently introduced, this tool has yet to illustrate improved diagnostic accuracy [40].

CBCT employs cone-shaped X-ray beams projected onto a flat panel detector system to produce cross-sectional multi-planar and 3D volumetric images in one single rotation of the source and detector around the patient. Volumetric intra-operative imaging, such as fixed and mobile CBCT, provide means to overcome CT-to-body divergence by providing feedback regarding the real-time tool–lesion relationship and allowing refinement of this relationship to assist in achieving TIL status. CBCT orbital scans, or spins, are best performed during a breath-hold manoeuvre to improve accuracy and minimise motion artefact [24]. Certain mechanical ventilation parameters are also effective in attenuating CT-to-body divergence and can be combined with intra-operative imaging modalities to further augment accuracy [25].

Several studies have demonstrated feasibility as well as higher rates of navigational success and diagnostic accuracy, albeit with varying diagnostic yield, when combining navigational bronchoscopy with CBCT technology [17, 18, 30, 31, 41]. Fixed CBCT platforms provide high-quality image resolution, but, depending on the institutional context and environment, may come at varying costs and require the use of a designated hybrid operating room [41, 42]. By combining electromagnetic navigation-based RAB with fixed CBCT, CUMBO-NACHELI *et al.* [18] reported a 100% TIL status and a 65% diagnostic yield rate in the sampling of 20 pulmonary lesions. STYRVOKY *et al.* [17] sampled 209 pulmonary lesions with a combination of ssRAB and augmented fluoroscopy CBCT platform with a reported diagnostic yield rate of 89%. The alternative platform of mCBCT provides the convenience of a mobile C-arm with volumetric imaging capabilities, albeit with an image resolution that is inferior to that of fixed CBCT platforms. CHAMBERS *et al.* [31] reported a 97% TIL rate with a diagnostic yield of 77% in 79 lesions targeted with the combination of ssRAB with a mobile O-arm CT (Medtronic, Minneapolis, MN, USA). Similarly, REISENAUER *et al.* [20] reported a TIL rate of 97% and a diagnostic yield of 93.3% in a prospective study of 30 lesions sampled by the combined use of ssRAB and mCBCT imaging. Our group previously reported an improvement in the tool–lesion relationship when combining mCBCT and ssRAB in the sampling of 10 lesions. Intra-operative volumetric imaging allowed for improvement of the tool–lesion relationship in three out of 10 instances and TIL was ultimately documented in nine out of 10 cases [19].

Across both cohorts in our current study, the diagnostic yield was 77% despite a 92% documented TIL rate. Interestingly, the diagnostic yield rates for the Primary Outcome (⩾2 spins) and the Comparison (0–1 spins) cohorts were not significantly different. The reason for this finding lies in the differences in

target lesion characteristics between the two cohorts. In general, target lesions in the Comparison cohort were larger and had a more favourable bronchus sign status and rpEBUS view (table 2). This indicates that the operator likely had sufficient confidence in sampling these lesions without CBCT imaging or by obtaining only one spin. In contrast, the only two significant procedure-related complications described in this study occurred in the Comparison cohort. The observed complication rate of 0.4% over 475 procedures in our combined cohort is lower than that reported in other studies [43]. With a high rate of CBCT imaging use in our study, this may suggest that CBCT imaging provides a more comprehensive spatial understanding of the thoracic anatomy and may assist in maintaining a safe distance from large blood vessels and the pleura prior to tissue acquisition.

Across the Primary Outcome cohort (⩾2 spins), the diagnostic yield was comparable for lesions in which TIL was documented on the last spin regardless of whether non-TIL or TIL were documented on the first spin (72% and 76%, respectively), while it was significantly lower at 40% for lesions in which TIL was not documented on the last spin. TIL status on the final mCBCT spin was associated with a 5-fold increase in the rate of diagnostic sampling in univariate and multivariate analysis models. Although this odds ratio was not statistically significant, likely owing to an underpowered number of observations, the direction of point estimates is aligned with our hypothesis and carries a clinical significance. It should also be noted that a diagnostic yield rate of 40% for documented non-TIL lesions is higher than expected and it can be postulated that in some of these cases a confirmatory spin was not obtained after final needle positioning.

Collectively, our data and that of others [17, 18, 20, 31] indicate that a 4–22% gap remains between the rates of TIL status and diagnostic yield. This implies that TIL is an imperfect surrogate for a diagnostic procedure. The reasons underlying non-diagnostic sampling despite intra-operative TIL status remain obscure and may represent the residual gap in diagnostic yield between RAB-guided and image-guided percutaneous sampling. The choice of sampling tools may explain some of this gap. While fine needles and small forceps are used commonly in RAB, percutaneous sampling allows for the use of coaxial core biopsy needles, which are likely to provide a higher volume of diagnostic material. Within that context, experience in the performance of cryo-biopsies *via* RAB is growing and may bridge some of this tissue volume gap [44–46].

Several limitations of this study warrant attention. Despite the intent to include all lesions sampled *via* ssRAB in which ⩾2 mCBCT spins were performed, 58 lesions were excluded from the analysis due to inadequate or partial image availability. Although technical in nature, elimination of those cases may introduce a degree of bias to the results. Having several operators from different training and experience backgrounds perform RAB introduces heterogeneity into the practice. Indeed, the performance of RAB in our institution has yet to be standardised and several aspects of the procedure, such as use of rpEBUS, use and number of mCBCT spins and sampling tool selection, are left to the discretion of the operator. This calls for internal standardisation of the RAB procedure based on institute-derived data for the purpose of continuous improvement in yield and safety. The interpretation of intra-operative volumetric imaging and the tool–lesion relationship may be prone to visual bias introduced by tool deployment, metal artefact and temporal differences in target characteristics between the pre-operative CT and intra-operative imaging. In the current study, we attempted to attenuate this bias by incorporating a dual independent observer review of the imaging to define the tool–lesion relationship. The overall generalisability of these findings could be affected by several factors, including the RAB platform employed, the CBCT platform used, the incorporation of rapid on-site evaluation into the workflow, the higher pre-test probability of malignancy in a cancer centre patient population and operator experience. Finally, recent advances in technology allow for the integration of the Ion ssRAB platform with the Cios Spin mCBCT to enhance attenuation of intra-operative CT-to-body divergence and potentially improve TIL status acquisition. Cases included in this study were performed prior to the formal integration. As the focus of an ongoing multicentre trial [47], it is possible that the outcomes described in the current study could hypothetically be improved with the latest integration of the two systems.

Interpretation

This is the first study to demonstrate a significant qualitative and quantitative improvement in achieving TIL status through the incorporation of ssRAB with mCBCT. Although achieving TIL status did not fully translate into a similar rate of diagnostic yield, the potential positive impact of volumetric intra-operative imaging on the diagnostic sampling was implied in lesions in the extreme low range of the diameter spectrum. Further prospective, multicentre studies are warranted to further confirm our findings and evaluate the relationship between intra-operative volumetric imaging and diagnostic yield as well as the gap between achievement of TIL status and diagnostic sampling.

References

1   Gould MK, Tang T, Liu IL, *et al.* Recent trends in the identification of incidental pulmonary nodules. *Am J Respir Crit Care Med* 2015; 192: 1208–1214.

2   Gould MK, Donington J, Lynch WR, *et al.* Evaluation of individuals with pulmonary nodules: when is it lung cancer? Diagnosis and management of lung cancer, 3rd ed: American College of Chest Physicians evidence-based clinical practice guidelines. *Chest* 2013; 143: Suppl. 5, e93S–e120S.

3   Steinfort DP, Khor YH, Manser RL, *et al.* Radial probe endobronchial ultrasound for the diagnosis of peripheral lung cancer: systematic review and meta-analysis. *Eur Respir J* 2011; 37: 902–910.

4   Gex G, Pralong JA, Combescure C, *et al.* Diagnostic yield and safety of electromagnetic navigation bronchoscopy for lung nodules: a systematic review and meta-analysis. *Respiration* 2014; 87: 165–176.

5   Folch EE, Labarca G, Ospina-Delgado D, *et al.* Sensitivity and safety of electromagnetic navigation bronchoscopy for lung cancer diagnosis: systematic review and meta-analysis. *Chest* 2020; 158: 1753–1769.

6   Ho ATN, Gorthi R, Lee R, *et al.* Solitary lung nodule: CT-guided transthoracic biopsy vs transbronchial biopsy with endobronchial ultrasound and flexible bronchoscope, a meta-analysis of randomized controlled trials. *Lung* 2023; 201: 85–93.

7   DiBardino DM, Yarmus LB, Semaan RW. Transthoracic needle biopsy of the lung. *J Thorac Dis* 2015; 7: Suppl. 4, S304–S316.

8   Ost DE, Ernst A, Lei X, *et al.* Diagnostic yield and complications of bronchoscopy for peripheral lung lesions. results of the AQuIRE registry. *Am J Respir Crit Care Med* 2016; 193: 68–77.

9   Folch EE, Pritchett MA, Nead MA, *et al.* Electromagnetic navigation bronchoscopy for peripheral pulmonary lesions: one-year results of the prospective, multicenter NAVIGATE study. *J Thorac Oncol* 2019; 14: 445–458.

10 Heerink WJ, de Bock GH, de Jonge GJ, *et al.* Complication rates of CT-guided transthoracic lung biopsy: meta-analysis. *Eur Radiol* 2017; 27: 138–148.

11 Agrawal A, Ho E, Chaddha U, *et al.* Factors associated with diagnostic accuracy of robotic bronchoscopy with 12-month follow-up. *Ann Thorac Surg* 2023; 115: 1361–1368.

12 Benn BS, Gmehlin CG, Kurman JS, *et al.* Does transbronchial lung cryobiopsy improve diagnostic yield of digital tomosynthesis-assisted electromagnetic navigation guided bronchoscopic biopsy of pulmonary nodules? A pilot study. *Respir Med* 2022; 202: 106966.

13 Chaddha U, Kovacs SP, Manley C, *et al.* Robot-assisted bronchoscopy for pulmonary lesion diagnosis: results from the initial multicenter experience. *BMC Pulm Med* 2019; 19: 243.

14 Kalchiem-Dekel O, Connolly JG, Lin IH, *et al.* Shape-sensing robotic-assisted bronchoscopy in the diagnosis of pulmonary parenchymal lesions. *Chest* 2022; 161: 572–582.

15 Low S-W, Lentz RJ, Chen H, *et al.* Shape-sensing robotic-assisted bronchoscopy vs digital tomosynthesis-corrected electromagnetic navigation bronchoscopy: a comparative cohort study of diagnostic performance. *Chest* 2023; 163: 977–984.

16 Pritchett MA, Bhadra K, Calcutt M, *et al.* Virtual or reality: divergence between preprocedural computed tomography scans and lung anatomy during guided bronchoscopy. *J Thorac Dis* 2020; 12: 1595–1611.

17 Styrvoky K, Schwalk A, Pham D, *et al.* Shape-sensing robotic-assisted bronchoscopy with concurrent use of radial endobronchial ultrasound and cone beam computed tomography in the evaluation of pulmonary lesions. *Lung* 2022; 200: 755–761.

18 Cumbo-Nacheli G, Velagapudi RK, Enter M, *et al.* Robotic-assisted bronchoscopy and cone-beam CT: a retrospective series. *J Bronchology Interv Pulmonol* 2022; 29: 303–306.

19 Kalchiem-Dekel O, Fuentes P, Bott MJ, *et al.* Multiplanar 3D fluoroscopy redefines tool–lesion relationship during robotic-assisted bronchoscopy. *Respirology* 2021; 26: 120–123.

20 Reisenauer J, Kern JD, Fernandez-Bussy R, *et al.* Combining shape-sensing robotic bronchoscopy with mobile three-dimensional imaging to verify tool-in-lesion and overcome divergence: a pilot study. *Mayo Clin Proc Innov Qual Outcomes* 2022; 6: 177–185.

21 Harris PA, Taylor R, Thielke R, *et al.* Research electronic data capture (REDCap) – a metadata-driven methodology and workflow process for providing translational research informatics support. *J Biomed Inform* 2009; 42: 377–381.

22 Casal RF, Sepesi B, Sagar AS, *et al.* Centrally located lung cancer and risk of occult nodal disease: an objective evaluation of multiple definitions of tumour centrality with dedicated imaging software. *Eur Respir J* 2019; 53: 1802220.

23 Seijo LM, de Torres JP, Lozano MD, *et al.* Diagnostic yield of electromagnetic navigation bronchoscopy is highly dependent on the presence of a bronchus sign on CT imaging: results from a prospective study. *Chest* 2010; 138: 1316–1321.

24 Pritchett MA, Lau K, Skibo S, *et al.* Anesthesia considerations to reduce motion and atelectasis during advanced guided bronchoscopy. *BMC Pulm Med* 2021; 21: 240.

25 Bhadra K, Setser RM, Condra W, *et al.* Lung navigation ventilation protocol to optimize biopsy of peripheral lung lesions. *J Bronchology Interv Pulmonol* 2022; 29: 7–17.

26 Kurimoto N, Miyazawa T, Okimasa S, *et al.* Endobronchial ultrasonography using a guide sheath increases the ability to diagnose peripheral pulmonary lesions endoscopically. *Chest* 2004; 126: 959–965.

27 GmbH SH. Cios Spin Operator Manual. Print No. ATSC-500.620.30.04.24. Erlangen, Germany, Siemens Healthineers GmbH, 2021.

28 Vachani A, Maldonado F, Laxmanan B, *et al.* The effect of definitions and cancer prevalence on diagnostic yield estimates of bronchoscopy: a simulation-based analysis. *Ann Am Thorac Soc* 2023; 20: 1491–1498.

29 Leonard KM, Low SW, Echanique CS, *et al.* Diagnostic yield versus diagnostic accuracy for peripheral lung biopsy evaluation: evidence supporting a future pragmatic endpoint. *Chest* 2024; 165: 1555–1562.

30 Benn BS, Romero AO, Lum M, *et al.* Robotic-assisted navigation bronchoscopy as a paradigm shift in peripheral lung access. *Lung* 2021; 199: 177–186.

31 Chambers J, Knox D, Leclair T. O-arm CT for confirmation of successful navigation during robotic assisted bronchoscopy. *J Bronchology Interv Pulmonol* 2022; 30: 155–162.

32 Chen A, Pastis N, Furukawa B, *et al.* The effect of respiratory motion on pulmonary nodule location during electromagnetic navigation bronchoscopy. *Chest* 2015; 147: 1275–1281.

33 Ye J, Zhang R, Ma S, *et al.* Endobronchial ultrasound plus fluoroscopy-guided biopsy compared to fluoroscopy-guided transbronchial biopsy for obtaining samples of peripheral pulmonary lesions: a systematic review and meta-analysis. *Ann Thorac Med* 2017; 12: 114–120.

34 Cheng GZ, Liu L, Nobari M, *et al.* Cone beam navigation bronchoscopy: the next frontier. *J Thorac Dis* 2020; 12: 3272–3278.

35 Hogarth DK. Use of augmented fluoroscopic imaging during diagnostic bronchoscopy. *Future Oncol* 2018; 14: 2247–2252.

36 Pritchett MA, Bhadra K, Mattingley JS. Electromagnetic navigation bronchoscopy with tomosynthesis-based visualization and positional correction: three-dimensional accuracy as confirmed by cone-beam computed tomography. *J Bronchology Interv Pulmonol* 2021; 28: 10–20.

37 Pritchett MA. Prospective analysis of a novel endobronchial augmented fluoroscopic navigation system for diagnosis of peripheral pulmonary lesions. *J Bronchology Interv Pulmonol* 2021; 28: 107–115.

38 Cicenia J, Bhadra K, Sethi S, *et al.* Augmented fluoroscopy: a new and novel navigation platform for peripheral bronchoscopy. *J Bronchology Interv Pulmonol* 2021; 28: 116–123.

39 Ali MS, Trick W, Mba BI, *et al.* Radial endobronchial ultrasound for the diagnosis of peripheral pulmonary lesions: a systematic review and meta-analysis. *Respirology* 2017; 22: 443–453.

40 Almeida FA, Salam S, Mehta AC, *et al.* Sampling utility of the convex probe endobronchial ultrasound visible intrapulmonary lesion. *J Bronchology Interv Pulmonol* 2018; 25: 290–299.

41 Chan JWY, Chang ATC, Yu PSY, *et al.* Robotic assisted-bronchoscopy with cone-beam CT ICG dye marking for lung nodule localization: experience beyond USA. *Front Surg* 2022; 9: 943531.

42 Setser R, Chintalapani G, Bhadra K, *et al.* Cone beam CT imaging for bronchoscopy: a technical review. *J Thorac Dis* 2020; 12: 7416–7428.

43   Ali MS, Ghori UK, Wayne MT, *et al.* Diagnostic performance and safety profile of robotic-assisted bronchoscopy: a systematic review and meta-analysis. *Ann Am Thorac Soc* 2023; 20: 1801–1812.

44   Oberg CL, Lau RP, Folch EE, *et al.* Novel robotic-assisted cryobiopsy for peripheral pulmonary lesions. *Lung* 2022; 200: 737–745.

45   Nasu S, Okamoto N, Suzuki H, *et al.* Comparison of the utilities of cryobiopsy and forceps biopsy for peripheral lung cancer. *Anticancer Res* 2019; 39: 5683–5688.

46   Arimura K, Tagaya E, Akagawa H, *et al.* Cryobiopsy with endobronchial ultrasonography using a guide sheath for peripheral pulmonary lesions and DNA analysis by next generation sequencing and rapid on-site evaluation. *Respir Investig* 2019; 57: 150–156.

47   A multicenter study to evaluate the Cios Spin and Ion Endoluminal System for pulmonary nodule biopsy. NCT05562895. https://clinicaltrials.gov/study/NCT05562895 Date last accessed: 26 January 2024.